Japanese Journal of Applied Physics

RAPID COMMUNICATIONS

Effects of carbon defects on ZnO nanorods directly grown on graphene

Japanese Journal of Applied Physics **56**, 110306 (2017)
https://doi.org/10.7567/JJAP.56.110306

RAPID COMMUNICATION

Effects of carbon defects on ZnO nanorods directly grown on graphene

Mitsuhiro Honda, Fuyuki Tokuda, and Yo Ichikawa

Graduate School of Engineering, Nagoya Institute of Technology, Nagoya 466-8555, Japan

Received July 19, 2017; accepted September 1, 2017; published online October 16, 2017

The correlation between carbon defects and the density of ZnO nanorods directly grown on graphene was studied. Thermal annealing was performed to vary the defect density of graphene on which ZnO nanorods were directly grown via hydrothermal synthesis. We found that ZnO nanorods were densely distributed on a highly defective graphene. Furthermore, specific defect sites were observed to provide upright ZnO nanorods. Raman spectroscopy revealed that the thermally induced defect corresponds to a carbon vacancy, which is expected to provide a reactive graphene surface where precursors can be easily attached to trigger the nucleation and further growth of ZnO nanorods. The local measurement of defects is believed to elucidate the key parameters for the growth of highly oriented ZnO nanorods.

The hybrid structure of graphene and inorganic nanomaterials is emerging as a novel material used to achieve high-performance and flexible optoelectronic devices.[1–3] Among the various types of hybrid materials, ZnO–graphene heterostructures have unfolded as an element of gas sensors or biosensors, lithium ion batteries, solar cells, and UV–vis optoelectronic devices.[4–6] Although a conventional way to fabricate ZnO–graphene is to synthesize ZnO nanomaterials on a seed layer deposited on graphene, the direct growth of ZnO on graphene has recently been reported in some papers.[7–10] Those studies presented the formation of ZnO nanorods, nanowalls, and thin films with high quality comparable to that of such nanomaterials grown by a conventional seed-mediated method. Although the key to the direct growth of ZnO nanomaterials on graphene was suggested to be the presence of graphene defects, which serve as nucleation sites to initiate the following growth of ZnO nanomaterials, the correlation between graphene defects and ZnO growth on them is still unclear.[8] In 2015, Park et al. presented the enhancement of ZnO nanowall formation on plasma-treated graphene; however, a graphene platform was disregarded and only ZnO products were characterized.[11] Studies on the effects of defects on ZnO nanorod growth, as well as the defect engineering of graphene, lead to precise control of the orientation and density of products. Herein, we studied the relationship between the density of graphene defects and the growth of ZnO nanorods.

Following the procedure in Ref. 7, few-layer graphene was synthesized on Cu foil (99.9%, 0.010 mm thick, $1 \times 1\,\mathrm{cm}^2$) by atmospheric chemical vapor deposition (APCVD) using camphor as a carbon source. 5 mg of camphor was evaporated at 200 °C and transported by a flow of H_2/Ar (10 : 190) gas mixture for 1 min onto Cu foil preliminarily annealed at 1000 °C for 1.5 h under H_2/Ar (20 : 80) gas-mixture flow. The graphene formed on a Cu foil was transferred onto a quartz substrate by a general wet transfer technique using poly(methyl methacrylate) (PMMA) solution.[7,12] To induce defects on the graphene structure, the samples were annealed at 400 °C under O_2 flow. The time for annealing was changed from 1 to 3 h to change the defect density. Each sample was characterized by UV–vis absorption spectroscopy (Shimadzu UVmini-1240), Raman spectroscopy (JASCO NRS-3300), and scanning electron microscopy (SEM; JEOL JSM-5600). Finally, ZnO nanorods were grown on graphene samples prepared via hydrothermal synthesis using a previously reported recipe.[7] The grown ZnO nanorods were observed by SEM.

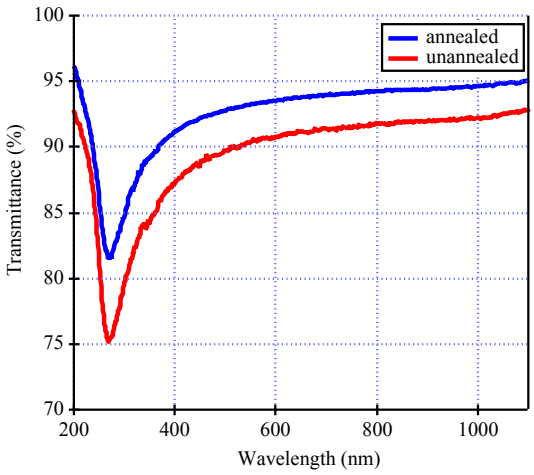

Fig. 1. (Color online) Transmittance spectra of graphene before (red) and after (blue) annealing under oxygen flow. The annealing time was 1 h.

Figure 1 shows the transmittance spectra of untreated (red) and annealed (blue) graphene samples. The main peaks seen at 260 nm in both samples are derived from C=C bonds in graphene.[13] After the thermal annealing of graphene in O_2 atmosphere, the graphene sample exhibited a higher transmittance. Since the presence of oxygen is in favor of forming defects, graphene is expected to be etched during annealing.[14]

Figure 2(a) shows the representative Raman spectra of graphene before and after annealing in O_2 atmosphere. In both samples, the characteristic Raman peaks of graphene are observed at 1360, 1580, and 2700 cm^{-1}, which are referred to as D, G, and 2D bands, respectively.[15] The D band is formed by disorder, while the G and 2D bands are indicative of sp2 in graphene. The peak at 1628 cm^{-1} is generally called the D′ band, whose intensity divided by the G band intensity ($I_D/I_{D'}$) enables us to estimate the type of defect.[16] By curve fitting using a Lorentz function, $I_D/I_{D'}$ is calculated to be ~6.1, signifying that carbon vacancies are defects formed by thermal treatment. The structure of graphene is expected to be locally distorted owing to the lack of carbon atoms.[17]

Figures 2(b)–2(e) show Raman maps constructed using the G band intensity and I_D/I_G values for graphene samples, where panels (b, d) and (c, e) denote graphene samples untreated and annealed in O_2, respectively. Before thermal treatment, graphene with fewer defects is seen in Figs. 2(b) and 2(d) to cover the substrate surface entirely and uniformly. After annealing, graphene is still seen to cover the entire substrate surface while the thorough distribution of defects is

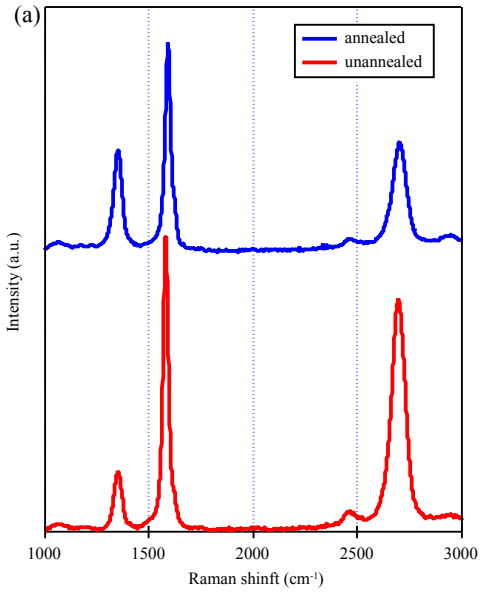

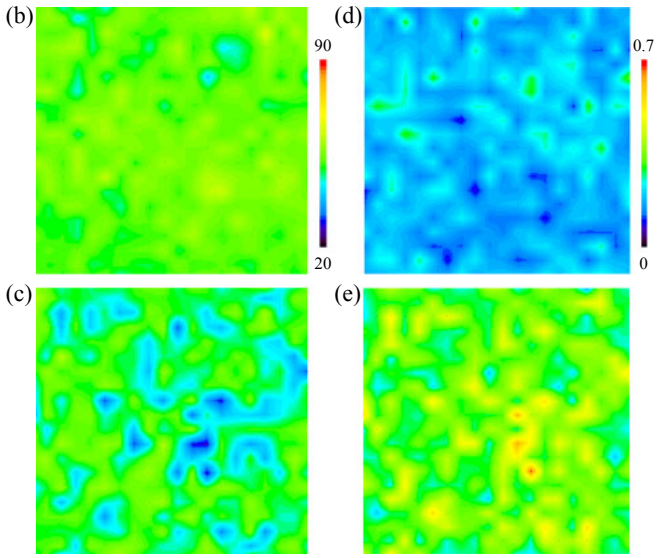

Fig. 2. (Color online) (a) Raman spectra and (b)–(e) Raman maps of graphene samples. Red and blue spectra in panel (a), and panels (b, d) and (c, e) denote graphene with and without annealing, respectively. Raman maps in panels (b, c) and (d, e) are constructed using the G band intensity and I_D/I_G values, where both vertical and horizontal lengths correspond to 280 μm.

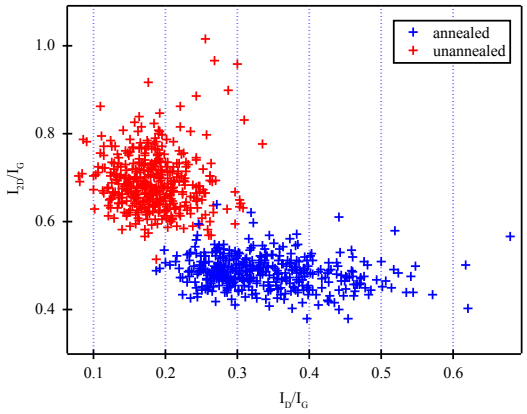

Fig. 3. (Color online) Distribution map for I_D/I_G and I_{2D}/I_G of untreated and annealed graphene samples, shown by red and blue symbols, respectively. For each sample, Raman spectra were measured at 400 points in an area of $280 \times 280\,\mu m^2$.

observed. Thus, by Raman spectroscopy, graphene etching by thermal annealing is confirmed to proceed over the entire surface, which is consistent with the higher transmittance observed in Fig. 1.

The Raman peak intensities of the D, G, and 2D bands measured at several points in the samples were analyzed to obtain the ratio of the D and 2D peak intensities to the G peak intensity. The ratio of the D peak intensity to the G peak intensity (I_D/I_G) is used to evaluate the density of defects. On the other hand, the ratio of the 2D peak intensity to the G peak intensity (I_{2D}/I_G) is usually used to estimate the number of graphene layers. In this study, the average of I_{2D}/I_G before annealing was determined to be 0.69, which indicates that the number of as-prepared graphene layers is 2 or 3. Figure 3 shows the relationship between I_D/I_G and I_{2D}/I_G for graphene samples. As shown in Fig. 2, the I_D/I_G of graphene annealed in O_2 atmosphere was clearly observed to be higher than that of untreated graphene. Moreover, the average I_D/I_G before annealing increased from 0.18 to 0.34 after annealing in O_2. Thus, graphene was damaged by C=C bond breaking during thermal annealing. In contrast, I_{2D}/I_G was observed to decrease after annealing. The reduction in I_{2D}/I_G indicates an increase in the number of graphene layers, which contradicts the observed results of transmittance and Raman mapping on first glance. From the viewpoint of the absence of a carbon resource during annealing, it is obvious that an increment in the number of graphene layers is improbable. The decrease in I_{2D}/I_G observed in our experiments is considered to be explained by the doping of gas molecules such O_2 or N_2 during or after annealing, as reported elsewhere.[18)]

The coverage of graphene samples annealed for different times was examined by SEM. Figure 4(a) shows the coverage of graphene samples untreated and annealed for different times. Insets are the SEM images of graphene on a quartz substrate obtained before (left) and after (right) annealing. In these images, graphene is observed as the dark area owing to its electrical conductivity, while the quartz substrate is observed as the bright area, which is formed by charge-up due to its electrical insulation. The coverage ratio of graphene was calculated from the dark area divided by the total observation area on the substrate. In Fig. 4(a), it is obvious that the coverage ratio of graphene drops suddenly after 1 h, indicating that etching is accelerated once graphene starts to be destructed.[18)]

Using graphene samples annealed for different times, Raman spectroscopy was performed at the point inside a graphene island to avoid the edge effect, and the results were analyzed to obtain I_D/I_G and I_{2D}/I_G. Figure 4(b) shows the annealing time dependence of I_D/I_G and I_{2D}/I_G of graphene. With longer annealing time, I_D/I_G is seen to increase linearly from 0.17 to 0.32, 0.47, and 0.55. Since I_D/I_G is proportional to the defect density, graphene is considered to become more defective with increasing annealing time. By contrast, I_{2D}/I_G is seen to be independent of annealing time, which is probably due to the rapid occupation of doping sites by surrounding gas molecules.

On the graphene samples with various defect densities, ZnO nanorods were grown and observed by SEM. Figures 5(a) and 5(b)–5(d) show the SEM images of ZnO

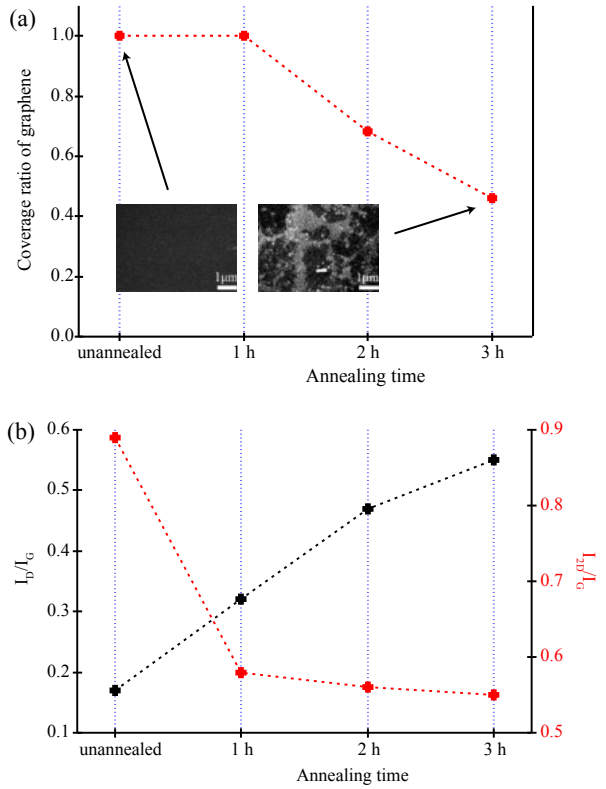

Fig. 4. (Color online) (a) Coverage ratio of graphene on a quartz substrate measured by SEM. Insets are the SEM images of graphene obtained before (left) and after (right) annealing for 3 h. (b) Effects of annealing time on I_D/I_G (black) and I_{2D}/I_G (red).

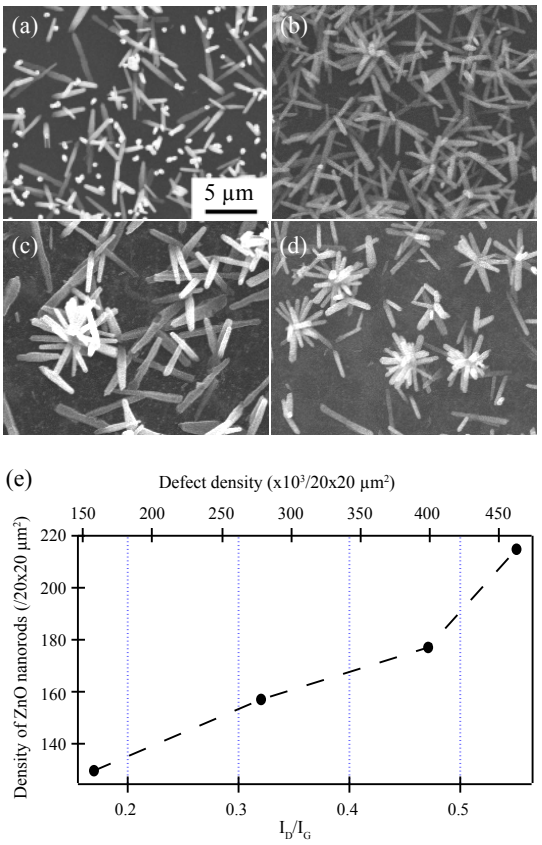

Fig. 5. (Color online) SEM images of ZnO nanorods grown on (a) untreated and (b)–(d) annealed graphene samples. Panels (b)–(d) indicate different annealing times of 1, 2, and 3 h, respectively. (e) Effects of I_D/I_G and defect density on the density of ZnO nanorods, as measured by SEM.

nanorods directly grown on graphene obtained before and after annealing, respectively. Panels (b)–(d) denote different annealing times of 1, 2, and 3 h, respectively. The specific nanorod growth at graphene edges was not observed in our experiments; hence, the effect of graphene edges on ZnO nanorod growth is not considered in this study, although graphene samples prepared by CVD typically include micrometer-sized grains with edges.[19] In Fig. 5(b), a graphene sample annealed for 1 h is clearly seen to provide ZnO nanorods with a density higher than those provided by the untreated graphene sample [Fig. 5(a)]. In graphene samples annealed for 2 and 3 h, ZnO nanorods with larger diameter are seen to be dominant although their density is slightly reduced. Their lower density is attributed to graphene removal from the substrate surface by longer annealing, as shown in Fig. 4. In fact, the growth of ZnO nanorods was not observed on a bare quartz substrate. Although graphene defects were vaguely recognized as nucleation sites, it is evidently suggested here that graphene defects (carbon vacancies) dictate the growth of ZnO nanorods.

From the SEM images measured at an oblique angle, the number of ZnO nanorods directly grown on graphene was counted to measure their density, where only the products dispersed on the grown nanorods were excluded. Note that several images were used here to make the measurement area of ZnO nanorods equivalent to that of graphene defects. The density of ZnO nanorods was obtained by dividing the number of ZnO nanorods by the graphene coverage. Figure 5(e) shows the relationship between I_D/I_G and ZnO nanorod density. The density of ZnO nanorods grown on graphene was observed to be linearly related to I_D/I_G. Taking into account that a higher I_D/I_G results from more defective graphene, the vacancy-type defects are considered to serve as nucleation sites for the initiation of nanorod growth. Indeed, structural distortions due to a lack of carbon atoms are known to provide a reactive surface, which generates preferential sites for the adsorption of chemical agents or precursors.[20] We expect that hydroxyl groups (OH^-) will be attached to those sites during hydrothermal synthesis, and thus, they serve as a trigger for ZnO nucleation and further nanorod growth. When we assume point-like defects that are separated from each other, the defect density can be calculated from $n_d\ (/cm^2) = 7.3 \times 10^9 \times EL^4\ [eV^4] \times I_D/I_G$, where EL is the energy of excitation light.[21,22] As indicated by the upper axis in Fig. 5(e), the highest defect density in our experiments is calculated to be $5 \times 10^5/20 \times 20\,\mu m^2$, which is much higher than the nanorod density of $2 \times 10^2/20 \times 20\,\mu m^2$. This finding explains that the density of nuclei for nanorod growth is much lower than that of defects. We expect that vacancies will be localized at one random point, and that a single nucleus will be formed on such a vacancy ensemble. As seen in Figs. 5(b)–5(d), most ZnO nanorods are observed to grow radially from specific points on defective graphene to form flower like nanorods and also to be thicker than those on less defective graphene. This is expected to be due to the higher reactivity of defect-concentrated sites on the graphene surface. Hydroxyl groups (OH^-) in the solution used during hydrothermal synthesis are expected to adsorb easily onto

defect localized sites, leading to an intense reaction to form larger seed crystals. Larger seed crystals tend to be polycrystals with multiple crystal faces, which suggest the growth of ZnO nanorods in various directions. Furthermore, the average diameter of ZnO nanorods is observed to be 430 nm on graphene with fewer defects ($I_D/I_G = 0.17$), and indeed, being somewhat larger, up to ~740 nm, on defective graphene. In contrast, in Fig. 5(a), some ZnO nanorods are found to be perfectly vertical to graphene. We expect that specific defects can provide vertically grown nanorods. Judging from the findings that upright ZnO nanorods are observed only on less defective graphene, point-like or tiny defect aggregates are speculated to be favorable for inducing a vertical orientation, although the local defect state and its correlation to ZnO growth are to be studied in more detail.

In conclusion, ZnO nanorods were grown on graphene with defects induced by thermal annealing in O_2 atmosphere. By Raman spectroscopy, the defects induced in graphene were identified to be carbon vacancies, and their density was increased by longer thermal treatment. On defective graphene, ZnO nanorods were grown preferentially, indicating that carbon vacancies serve as nucleation sites for ZnO nanorod growth. In addition, upright ZnO nanorods were found as a minor product, suggesting that specific defects allow for the growth of well-aligned products on graphene, although such defects are to be defined distinctively. The production of graphene with defined defects will enable us to control the morphology and alignment of ZnO nanomaterials for applications of ZnO/graphene hybrid nanostructures to functional devices.

Acknowledgement This research was supported by a Grant-in-Aid for Scientific Research from the Japan Society for the Promotion of Science (No. 26390102).

1) F. Huang, F. Jia, C. Cai, Z. Xu, C. Wu, Y. Ma, G. Fei, and M. Wang, Sci. Rep. **6**, 28943 (2016).
2) F. H. L. Koppens, T. Mueller, Ph. Avouris, A. C. Ferrari, M. S. Vitiello, and M. Polini, Nat. Nanotechnol. **9**, 780 (2014).
3) Q. Xiang, J. Yu, and M. Jaroniec, Chem. Soc. Rev. **41**, 782 (2012).
4) Y. Zhao, W. Li, L. Pan, D. Zhai, Y. Wang, L. Li, W. Cheng, W. Yin, X. Wang, J.-B. Xu, and Y. Shi, Sci. Rep. **6**, 32327 (2016).
5) Aaryashree, S. Biswas, P. Sharma, V. Awasthi, B. S. Sengar, A. K. Das, and S. Mukherjee, ChemistrySelect **1**, 1503 (2016).
6) M. Saranya, R. Ramachandran, and F. Wang, J. Sci.: Adv. Mater. Devices **1**, 454 (2016).
7) M. Honda, R. Okumura, and Y. Ichikawa, Jpn. J. Appl. Phys. **55**, 080301 (2016).
8) J. Liu, R. Liu, G. Xu, J. Wu, P. Thapa, and D. Moore, Adv. Funct. Mater. **23**, 4941 (2013).
9) N. S. A. Aziz, M. R. Mahmood, K. Yasui, and A. M. Hashim, Nanoscale Res. Lett. **9**, 95 (2014).
10) S. B. Ambade, R. B. Ambade, W. Lee, R. S. Mane, S. C. Yoon, and S.-H. Lee, Nanoscale **6**, 12130 (2014).
11) S. I. Park, Y. Tchoe, H. Baek, J. Heo, J. K. Hyun, J. Jo, M. Kim, and N. Jung, APL Mater. **3**, 016103 (2015).
12) X. Li, Y. Zhu, W. Cai, M. Borysiak, B. Han, D. Chen, R. D. Piner, L. Colombo, and R. S. Ruoff, Nano Lett. **9**, 4359 (2009).
13) Y. Gui, J. Yuan, W. Wang, J. Zhao, J. Tian, and B. Xie, Materials **7**, 4587 (2014).
14) Y. Lin, C. Lu, C. Yeh, C. Jin, K. Suenaga, and P. Ciu, Nano Lett. **12**, 414 (2012).
15) A. C. Ferrari, J. C. Meyer, V. Scardaci, C. Casiraghi, M. Lazzeri, F. Mauri, S. Piscanec, D. Jiang, K. S. Novoselov, S. Roth, and A. K. Geim, Phys. Rev. Lett. **97**, 187401 (2006).
16) A. Eckmann, A. Felten, A. Mishchenko, L. Britnell, R. Krupke, K. S. Novoselov, and C. Casiraghi, Nano Lett. **12**, 3925 (2012).
17) R. Faccio, L. Fernández-Werner, H. Pardo, C. Goyenola, O. N. Ventura, and Á. W. Mombrú, J. Phys. Chem. C **114**, 18961 (2010).
18) V. Kiisk, T. Kahro, J. Kozlova, and L. H. Alles, Appl. Surf. Sci. **276**, 133 (2013).
19) C. Mattevi, H. Kim, and M. Chhowalla, J. Mater. Chem. **21**, 3324 (2011).
20) F. Banhart, J. Kotakoski, and A. V. Krasheninnikov, ACS Nano **5**, 26 (2011).
21) X. Yu, Y. Shen, T. Liu, T. Wu, and Q. J. Wang, Sci. Rep. **5**, 12014 (2015).
22) M. Bruna, A. K. Ott, M. Ijäs, D. Yoon, U. Sassi, and A. C. Ferrari, ACS Nano **8**, 7432 (2014).